Research on Concrete Early Shrinkage Characteristics Based on Machine Learning Algorithms for Multi-objective Optimization

Authors: Jianqun Wang[1], Heng Liu[2,1], Junbo Sun[3,4*], Bo Huang[1], Yufei Wang[5,3], Hongyu Zhao[6], Mohamed Saafi[7], Xiangyu Wang[3**]

Jianqun Wang [1], Professor
[1] Hunan Provincial Key Laboratory of Structures for Wind Resistance and Vibration Control, Hunan University of Science and Technology, Xiangtan 411201, China;
E-mail address: jqw@hnust.edu.cn

Heng Liu [2,1], Master
[2] Hubei Jiaotou Jingchu Construction Management Co., Ltd, Wuhan 430051, China;
[1] Hunan Provincial Key Laboratory of Structures for Wind Resistance and Vibration Control, Hunan University of Science and Technology, Xiangtan 411201, China;
E-mail address: 1515510884@qq.com

Junbo Sun[3,4*], PhD, Senior Researcher
[3]School of Civil Engineering and Architecture, East China Jiao Tong University, Nanchang, 330013, China;
[4]Institute for Smart City of Chongqing University in Liyang, Chongqing University, Jiangsu, 213300, China;
E-mail address: tunneltc@gmail.com

Bo Huang [1], PhD, Lecturer
[1] Hunan Provincial Key Laboratory of Structures for Wind Resistance and Vibration Control, Hunan University of Science and Technology, Xiangtan 411201, China;
E-mail address: Bohuang@hnust.edu.cn

Yufei Wang[5,3], PhD, PhD Candidate
[5] School of Design and Built Environment, Curtin University, Perth, WA 6102, Australia;
[3] School of Civil Engineering and Architecture, East China Jiao Tong University, Nanchang, 330013, China;
E-mail address: wangyf0113_suz@163.com

Hongyu Zhao[6], PhD, PhD Candidate
[6] School of Civil Engineering, Chongqing University, Chongqing, 400045, China
E-mail address: 20211601069@cqu.edu.cn

Mohamed Saafi [7], PhD, Professor
[7] Department of Engineering, Lancaster University, Lancaster, LA1 4YR, UK;
E-mail address: m.saafi@lancaster.ac.uk

Xiangyu Wang[3**], PhD, Professor
[3] School of Civil Engineering and Architecture, East China Jiao Tong University, Nanchang, 330013, China;
E-mail address: Xiangyu.Wang@curtin.edu.au

Corresponding author: Junbo Sun, E-mail address: tunneltc@gmail.com

Abstract

Cracking phenomena in tunnel side wall structures (TSWS) increasingly jeopardize their longevity due to water leakage, reinforcement corrosion, and eventual collapse. The primary contributor, early-age shrinkage (EAS) induced by hydration reactions, significantly undermines structural stability and durability. The integration of expansion agents (EA) and fibers presents a low-cost, efficient strategy to counteract EAS-induced cracking. Despite its promise, limited research on the influencing factors constrains its broader application. This study delves into the impacts of EA content, the CaO-MgO ratio, and fiber reinforcement on flexural strength (FS), compressive strength (CS), and EAS, revealing a complex interplay where EA and CaO content detrimentally affect mechanical properties yet beneficially influence EAS. Results showed that EA and CaO content had negative effects on the mechanical properties, but had positive effect on EAS. Additionally, Random Forest (RF) was developed with hyperparameters refined via the firefly algorithm (FA) based on the experimental data. The validity of the built RF-FA models was verified by substantial correlation coefficients and low root-mean-square errors. Subsequently, a coFA-based firefly algorithm (MOFA) was proposed to optimise tri-objectives of mechanical properties, EAS, and cost simultaneously. The Pareto fronts were obtained effectively for the optimal mixture design. This study contributes to its practical implications, offering a scientifically grounded approach to enhancing TSWS concrete design for improved performance and durability.

Keywords: Expansion agent; CaO content; Mechanical properties; Early age shrinkage; Machine learning; Multi-objective optimisation

1. Introduction

Various tunnel are widely applied in urban underground space, sea floor, and mountains due to its space-free and versatile-conditions-compatibility[1-4]. However, cracking-related issues in tunnel side wall structures (TSWS), such as water leakage, reinforcement corrosion, and wall collapse, increasingly threaten structural durability. Among these issues, early age shrinkage caused by hydration reactions constitutes the majority, significantly impacting the stability and durability of structures [5]. Furthermore, additional challenges in mitigating the risk of thermal cracking include the large geometry of structures and the core-ambient temperature gradient [6-8]. Traditionally, strategies such as raw material pre-cooling and circulating water cooling have been employed to reduce cracking, but their high costs in terms of both economics and time hinder widespread application [9-11]. Consequently, there is a significant demand for optimization methodologies, such as the use of fiber in concrete and expansion agents [12-14].

Currently, research indicates that incorporating fiber into concrete is an effective strategy for reducing early age shrinkage cracking, offering benefits in terms of both cost-efficiency and implementation time [15-17]. Specifically, polypropylene fibers (including synthetic and hybrid types) and steel fibers are highlighted for their high tensile strength, lightweight, and affordability [18-20]. Yuan et al. [21] have noted that fibers significantly enhance both early age shrinkage and compressive performance. Alida et al. [22] denoted polypropylene fiber obviously give rise to the width and length reduction of the cracks during the first 24h cast procedure. However, mono addition of fiber still face challenge because its early age shrinkage effect would be damaged upon fiber ratio is under 1kg/m^3 while the concrete workability would be ruined if ratio exceed 0.8kg/m^3[23, 24]. Consequently, combining fibers with expansion agents emerges as a viable approach to optimizing both early age shrinkage performance and concrete workability [25-27].

Expansive agents, particularly those based on MgO, have garnered interest for their self-expansive properties, enhancing early-age shrinkage deformation, fluidity, microstructure, and mechanical performance [28-31]. Research by Wang et al. [32] on the effects of CaO-MgO ratios on the deformation and mechanical properties of expansive agent-infused concrete revealed that mixes containing both MgO and CaO exhibit pronounced expansion as the CaO-MgO ratio increases. The growth pressure of CaO crystals contributes to the expansion of the paste and increased porosity, counteracting early-age autogenous shrinkage while potentially reducing strength [33-37]. However, the cumulative effects of CaO, MgO, and fiber content on early-age shrinkage and the mechanical properties of concrete warrant further exploration to fully understand their interactive impacts.

To this end, the synergistic effects of CaO, MgO expansive agents, and fibers on the strengths and early-age autogenous shrinkage of TSWS were thoroughly investigated. However, the experimental procedures required significant effort to procure comprehensive results due to the numerous variables and the substantial workload and resources involved. Consequently, machine learning (ML) were explored to discern underlying patterns and applied to analyze the experimental data [38-40]. Random Forests (RF), known for their computational efficiency and excellent generalization capabilities, were employed as a key ML approach. Furthermore, the RF model demonstrated exceptional performance in preventing overfitting and exhibiting a high tolerance for outliers [41-43].

However, the performance of RF models is often constrained by their sensitivity to hyperparameters, a limitation that can be mitigated by optimization algorithms, thus moving beyond traditional methodologies [44-46]. Consequently, the Firefly Algorithm (FA) emerged as an optimal solution due to its ability to eliminate multimodality and facilitate automatic parameter tuning [47-49]. Therefore, FA was employed to optimize the hyperparameters of the RF model (FA-RF), with the goal of identifying optimal concrete mixtures by balancing general production costs against the performance characteristics of TSWS concrete. As a result, multi-objective optimization (MOO) models have been developed using metaheuristic algorithms employing Pareto methods to achieve optimized objectives [50-52]. Zhang et al. [53] successfully applied MOO models to meet the optimized requirements for cost, slump, and strength in plastic-concrete. Building on this methodology, the FA-RF model was extended to a multi-objective optimization framework (MOFA-RF) to optimize three critical aspects of TSWS concrete: cost, early-age autogenous shrinkage, and mechanical performance.

In this research, TSWS mixtures were developed utilizing MgO, CaO, and fiber content to examine the synergistic effects on early-age autogenous shrinkage and mechanical properties, including compressive and flexural strengths, across various ratios. The dataset comprised 216 groups detailing compressive strength and early-age shrinkage results, as detailed in the Appendix. Following the acquisition of Pareto front solutions, the MOFA-RF model was validated for application in the tri-objective mixture design of TSWS.

2. Experimental configuration

2.1 Raw materials

The fibers utilized in the experiment were from Nanjing Subrote Company, and the expansive agent was from Wuhan Sanyuan Company. The expansive agent was composed of CaO and MgO, both in powder form and added in a specific proportion. In this study, a polypropylene fiber with a length of 9mm and a diameter of 0.019mm was employed. The density of the fibers was 0.91-0.95 g/cm^3, and the tensile strength was greater than 500MPa. The test concrete used ordinary silicate cement with a grade of 40 MPa. Natural sand was used as the fine aggregate, with a particle size ranging from 2.4 to 2.8mm.

2.2 Mixture design

CaO, MgO, and fiber content are fully explored as the main variables of TSWS (Tailored Sulfur-Modified Wellbore Strengthening) mechanical properties (compressive and flexural strengths) and early age autogenous shrinkage. Expansive agent ranging from 1% to 1.6% declines early age shrinkage of TSWS mixture. Three CaO/MgO ratios (9:1, 8:2, 7:3) were set to be explored. Fiber was designed between 0.6-1kg/m3 to offer optimal stabilization efficiency and adequate workability. Hence, CaO to MgO ratio, and fiber content with specific ratios are shown in Table 1. As so, 243 TSWS specimens were prepared for the mechanical properties tests, and an additional 81 specimens were prepared specifically for shrinkage tests. In total, three ratios for expansion agent, fiber content, and CaO to MgO ratio, and three levels for age were involved in this research.

Table 1. 27 Group mix design.

Cement	Flyash	Expansion agent	MgO/CaO	Fiber	Sand	Stone	Water	Superplasticizer
260	125	26	1/9	0.6	766	1078	149	7.1
260	125	26	2/8	0.6	766	1078	149	7.1
260	125	26	3/7	0.6	766	1078	149	7.1
260	125	26	1/9	0.8	766	1078	149	7.1
260	125	26	2/8	0.8	766	1078	149	7.1
260	125	26	3/7	0.8	766	1078	149	7.1
260	125	26	1/9	1	766	1078	149	7.1
260	125	26	2/8	1	766	1078	149	7.1
260	125	26	3/7	1	766	1078	149	7.1
260	125	33	1/9	0.6	766	1078	151	7.1
260	125	33	2/8	0.6	766	1078	151	7.1
260	125	33	3/7	0.6	766	1078	151	7.1
260	125	33	1/9	0.8	766	1078	151	7.1
260	125	33	2/8	0.8	766	1078	151	7.1
260	125	33	3/7	0.8	766	1078	151	7.1
260	125	33	1/9	1	766	1078	151	7.1
260	125	33	2/8	1	766	1078	151	7.1
260	125	33	3/7	1	766	1078	151	7.1
260	125	40	1/9	0.6	766	1078	154	7.1
260	125	40	2/8	0.6	766	1078	154	7.1
260	125	40	3/7	0.6	766	1078	154	7.1

260	125	40	1/9	0.8	766	1078	154	7.1
260	125	40	2/8	0.8	766	1078	154	7.1
260	125	40	3/7	0.8	766	1078	154	7.1
260	125	40	1/9	1	766	1078	154	7.1
260	125	40	2/8	1	766	1078	154	7.1
260	125	40	3/7	1	766	1078	154	7.1

2.3 Sample preparation

Generally, the obtention of concrete early age autogenous shrinkage faces challenge for the displacement is tiny. Therefore, an self-manufactured element autogenous shrinkage test specimen (Fig. 1) was designed to address the difficulty in installing displacement sensors and obtaining key aspects of displacement in a representative and proper location. This apparatus was utilized to determine concrete relative displacement and early age shrinkage because the micrometer was capable of accurating to 0.001mm compared to 400mm long test cell.

The raw materials in this research include cement, water, and expansion agent, which were calculated based on designing ratios (expansion agent content, CaO/MgO ratio). Before the addition of water, cement and dry expansion agent were mixed for 60 seconds to ensure uniformity. The designed water content was then blended with other dry components for 480 seconds, before the dampened cement blend was transferred into the molds. For the mechanical properties tests, specimens were cured for aging periods of 3 days, 14 days, and 28 days. For shrinkage performance tests, the timing began from the initial setting of the specimens, with a testing duration of 5 days.

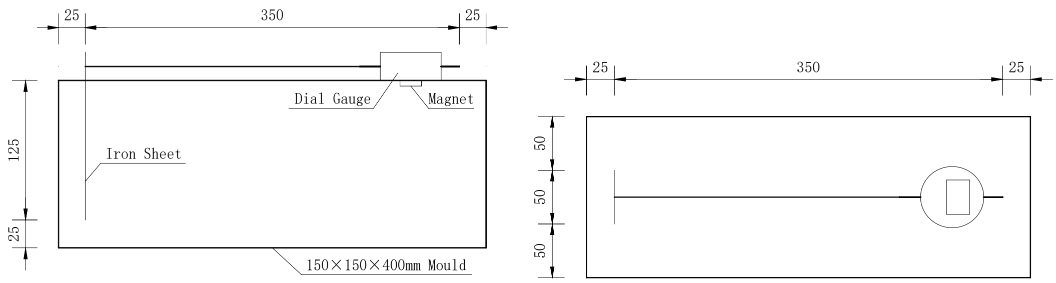

Fig. 1. Shrinkage test device.

2.4 Shrinkage test

Prior to the pouring of mixtures, a plastic film, treated with lubricants to ensure its smoothness, was positioned within the test specimen. This preparatory step was crucial in reducing the boundary friction, thereby minimizing its potential negative impact on the accuracy of autogenous shrinkage measurements. Afterwards, the TSWS mixtures were vibrated and densified at size of 150×150×400mm molds. To ensure that the shrinkage tests were conducted under consistent conditions, the ambient environment within the testing facility was meticulously controlled. The humidity (60±5%) and temperature (20±2℃) of the room were kept stable, providing a constant environment for the specimen throughout the testing period. An iron plate and strong magnet were installed in the specimen middle, 25mm and 75mm away from both ends. The iron plate was embedded 125mm deep in the specimen, and the micrometer was fixed by the strong magnet adsorbed on the concrete surface. After micrometer value was stable, micrometer was zeroed and then measured the shrinkage.

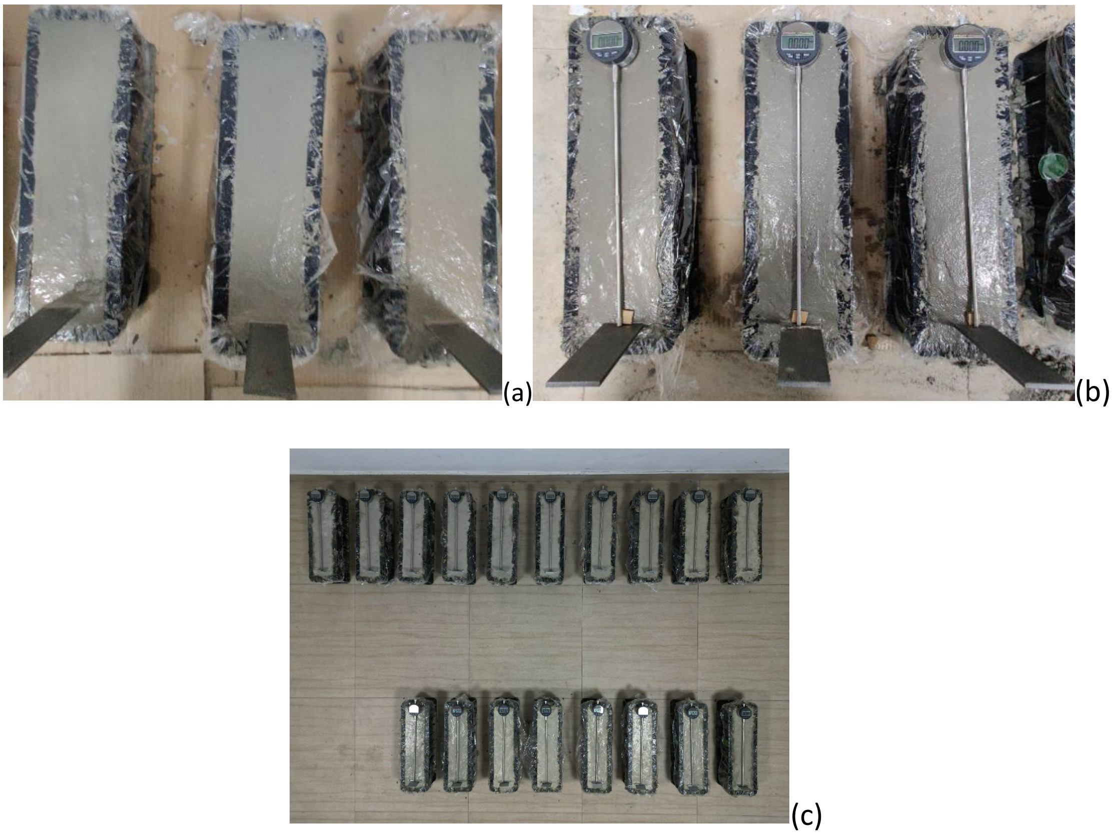

Fig. 2. Shrinkage device installation, (a) iron sheets and strong magnets installation, (b) micrometer installation, (c) shrinkage test

2.5 Splitting tension and Compressive strength test

The splitting tensile and compressive strength properties were determined using a special fixture (15 cm side length) placed on the TYA-2000S Electro-Hydraulic compressor in Fig. 3. The compressor load rate was controlled at 0.7MPa/s (compressive strength test) and 0.07Mpa/s (splitting tension test) until the deformation is destroyed, determining the compressive strength and splitting tensile capacity.

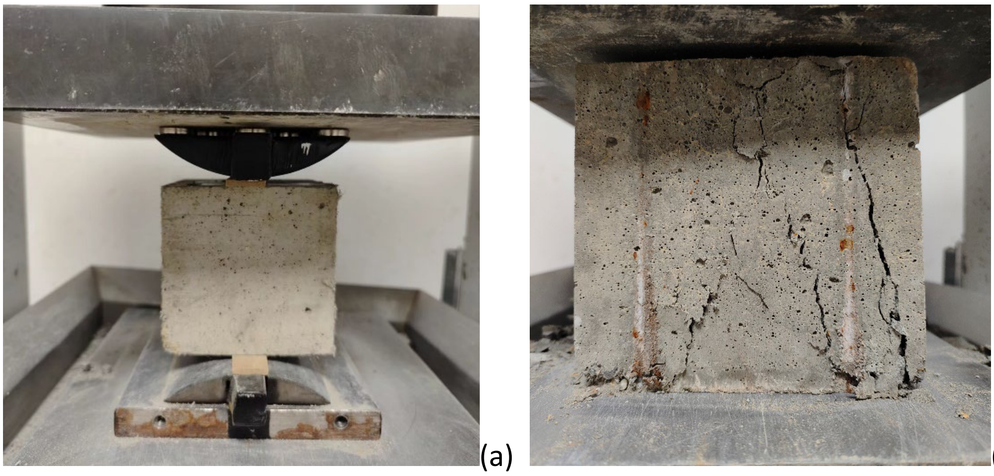

(a) (b)

Fig. 3. Mechanical properties test, (a) Splitting tensile test fixture, (b) compressive strength test.

3. Multi-objective-optimisation model method

A schematic of the multi-objective-optimization model approach employed for attaining the optimal TSWS mixtures with MOFA-RF operation was presented in Fig. 4. The initial phase entails three RF-proposition models for anticipating compressive strength, flexural strength, and early age shrinkage. During the process, 10-fold cross-validations (CV) and FA algorithm were used to adjust two hyperparameters of RF, namely the minNumLeaf and the numTree. Meanwhile, the cost of mixtures were determined by density of raw materials, such as MgO, CaO, and cement, etc. and defining the cost. Then, the MOFA was optimized the tri-objective design for TSWS, with a weighted sum method being utilized for the three-objectives. As so, the Pareto-front was constructed to confirm the TSWS enhancement mixture scheme. Both the optimisation experiments and ML model were carried out by means of Matlab R2020a.

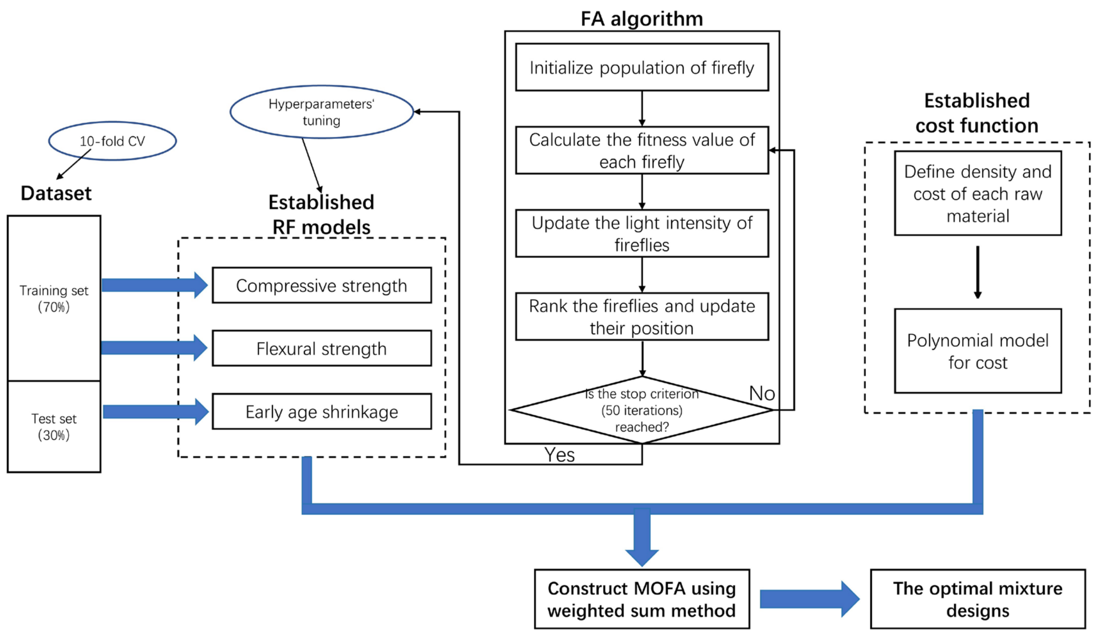

Fig. 4. Schematic descriptions of MOFA-RF model system to achieve optimized TSWS.

3.1 Data description

The mass ratio of materials were calculated by the variables of CaO, MgO and fiber content. The outputs were the flexural strength, compressive strength, and early age shrinkage with their associated data sets coming from the mechanical experiments. Table 2 provided a summary of basic datasets information including flexural strength, compressive strength, raw materials and early age shrinkage.

Table 2 Output and Input variables

variables	Maximum	Minimum	Mean	Medium	Std Dev	CV
CaO (kg/m^3)	36	18.2	26.4	26.4	5.43	0.21
MgO (kg/m^3)	12	2.6	6.6	6.6	3.02	0.46
Fiber (kg/m^3)	1	0.6	0.8	0.8	0.17	0.21
Compressive strength (kg/m^3)	51.3	22.1	35.3	36.5	9.40	0.27
Flexural strength (kg/m^3)	3.74	2.21	2.86	2.88	0.43	0.15
Early age shrinkage ($\times 10^{-6}$%)	1007	512	738.07	730	121.33	0.16

The correlations between input variables were demonstrated in Fig. 5 based on the flexural strength, compressive strength, and early-age-shrinkage. Only one matrix of mechanical performance relatedness was provided since the experimental mixed design of these three output variables was consistent. A correlation matrix was exploited to visualize the mutual influence between input variables, manifesting the Pearson correlation coefficient between the pairs of variables. Pearson Correlation Coefficient has proved to be a promising approach for assessing the association between X and Y. 0.5 was determined as the threshold for correlations between various components, suggesting that the input variables had little likelihood of triggering multicollinearity issues. The correlation coefficient between MgO and CaO was nearly 0.5, with the rest hovering around 0 since the ratio of MgO/CaO was set to 1/9, 2/8 and 3/7, while the other variables remained independent. The multi-objective optimization RF-FA model was then proposed.

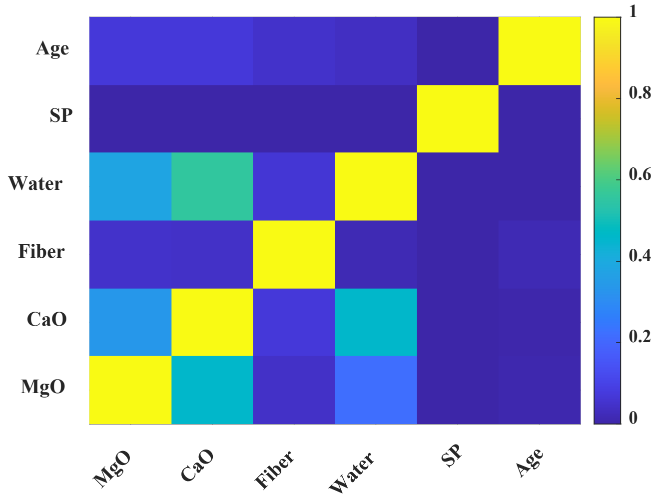

Fig. 5. Correlation chart of factors impacting mechanical performance.

3.2 Development of FA-RF models

3.2.1 Random forests

Random Forests (RF) implemented the final decision by creating hundreds of decision trees (RTs). Random Forests models apply the 'bagging' approach to combine the results from the RTs and obtain the peak results through voting in Fig. 6, which successfully improved the prediction performance and reduced the prediction variance[54]. Equation (1) presented the training sample Rn, involving output scalar and input variables with m features ($X = \{x_1, x_2, ..., x_m\}$), respectively.

During the processes of training each decision RTs, n sample are randomly sampled without replacement from the training set. The sampling process was referred to as 'bootstrap', and the bootstrap sample set was denoted by R_n^{θ} . Thereafter, the algorithm divided the input dataset R_n^{θ} . Upon conclusion of the RTs training sessions, the forecasting capability $\hat{a}(\mathrm{X}, R_n^{\theta})$ was formulated. Random Forests consist of *k* uncorrelated RTs, thereby forming k prediction-functions $\hat{a}(\mathrm{X}, R_n^{\theta_n})$, with the range of k being from 1 to k and R_n^{θ} being independent random vectors for distinguishing decision trees.

As so, the RF generates k outputs $\{\mathrm{Y}_1, \mathrm{Y}_2, ..., \mathrm{Y}_k\}$, respectively corresponding to each RT, and then takes the average of these output according to equation (2) to obtain the prediction value Y.

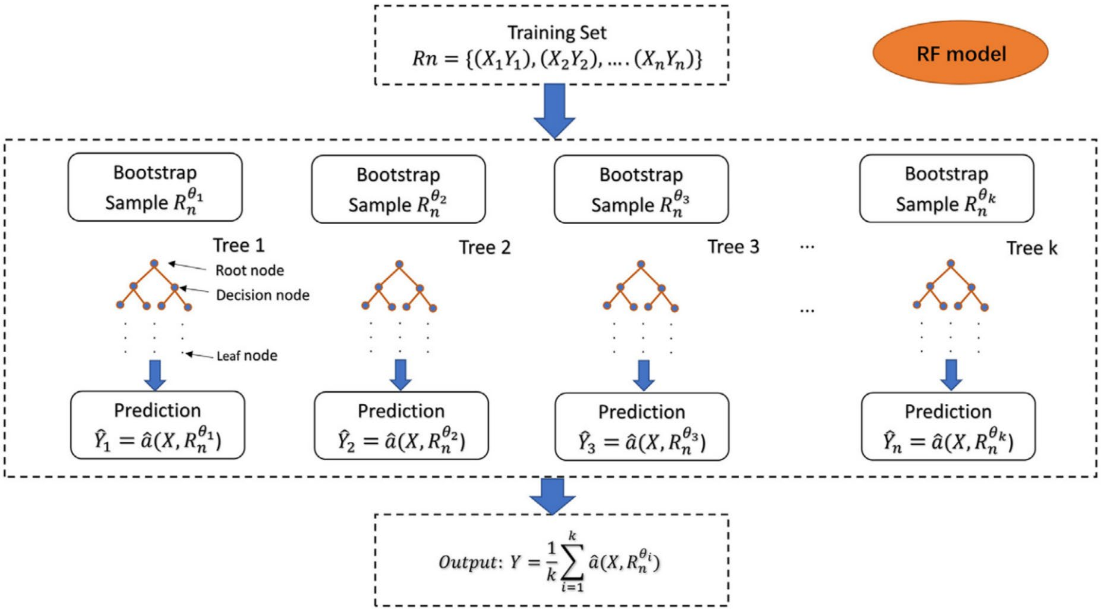

Fig. 6. Construction of an RF model.

$$R_n = \{(X_1, Y_1), (X_2, Y_2), \ldots., (X_n, Y_n)\} \tag{1}$$

$$Y = \frac{1}{k}\sum_{i=1}^{k} \hat{a}(X, R_n^{\theta_i}) \tag{2}$$

3.2.2 Firefly algorithm (FA) model

Fireflies are exhibit social behavior as they are drawn to light, and thus, so that the attractiveness of fireflies to others is positive to its brightness[55]. However, the brightest fireflies flit about sporadically, and as the gap between two of them grows the allure of the light fades. Other fireflies would constantly move towards the brightest firefly, which would eventually be seen. The brightness of firefly, which was measured by its objective function, altered when it got close (brighter) to firefly j, as evidenced by Equation (3).

$$x_i^{t+1} = x_i^t + \beta_0 e^{-\gamma r_{ij}^2}\left(x_j^t - x_i^t\right) + \alpha(\mathrm{rand} - 1/2) \tag{3}$$

$$r_{ij} = \left\| x_j^t - x_i^t \right\| \tag{4}$$

In the above function, the positions of fireflies i and j at the t-th iteration were x_i^t and x_j^t. In equation (4), r_{ij} showed Euclidean distances among two fireflies, and β_0 denoted the highest attraction of fireflies (r=0). Considering the medium brightness and the attenuation caused by distance, a value of was taken as the absorption coefficient, with a range from 0 to 1. Concurrently α and rand were assigned parameters and vectors randomly from a Gaussian-distribution, span from 0 to 1.

3.3 Cross fold verification

The complexity of the problem resulting from a limited amount of data being overfitted was solved by employing 10-fold cross-validation, as demonstrated in Fig. 7. First, the data were split into two parts randomly: training samples and test samples, accounting for 70% and 30% of the whole datasets respectively. The training samples were equally separated into 10 sets, out of which nine (internal-training-sets) were employed for models training. The remaining sets (validation-set) were utilized to evaluate the root-mean-square-error (RMSE) value. While training the model, 50 iterations of adjusting the hyperparameters were conducted for obtaining the minimal-RMSE with FA. The model was obtained through a validation process in which it was trained ten times. The model with the lowest RMSE value was selected as the most desirable model to further analyze its output on the test sets.

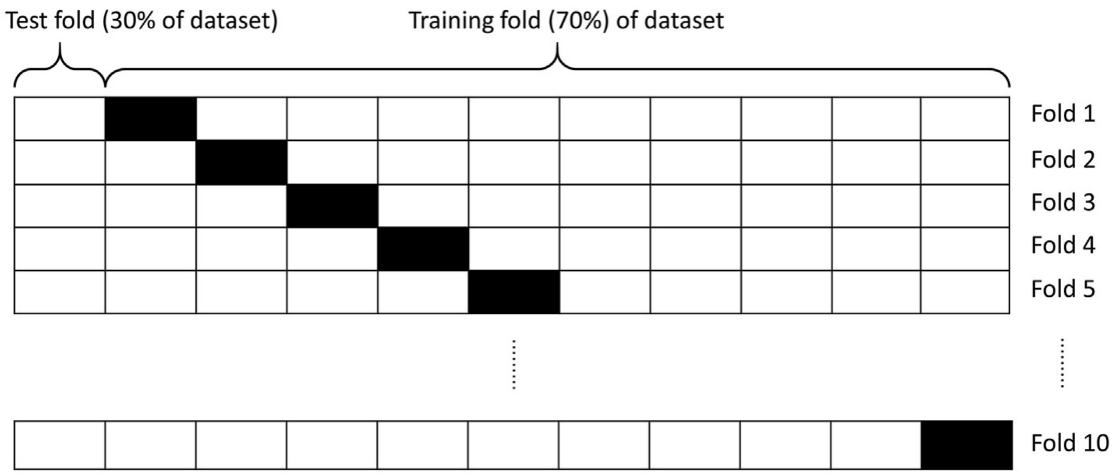

Fig. 7. training and test samples 7 10-Fold cross-validation.

In this investigation, four different metrics were adopted to evaluate the characteristic of ML models, which were RMSE, Correlation Coefficient (R), Mean Absolute Percentage Error (MAPE) and Mean Absolute Error (MAE).

$$\mathrm{RMSE} = \sqrt{\frac{1}{N}\sum_{i=1}^{N}\left(y_i^* - y_i\right)^2} \tag{5}$$

$$\mathrm{R} = \frac{\Sigma_{\mathrm{i}-1}^{N}\left(y_{\mathrm{i}}^* - \overline{y}^*\right)\left(y_{\mathrm{i}} - \overline{y}\right)}{\sqrt{\Sigma_{\mathrm{i}=1}^{N}\left(y_{\mathrm{i}}^* - \overline{y}^*\right)^2}\sqrt{\Sigma_{\mathrm{i}=1}^{N}\left(y_{\mathrm{i}} - \overline{y}\right)^2}} \tag{6}$$

$$\mathrm{MAPE} = \frac{1}{N}\sum_{i=1}^{n}\left|\frac{y_i^* - y_i}{y_i}\right| \tag{7}$$

$$\mathrm{MAE} = \frac{1}{N}\sum_{i=1}^{n}\left|y_i^* - y_i\right| \tag{8}$$

where *N* denote the specimen of quantity in the dataset, y_i^* represent the prediction output value of the machine learning model, y_i represent the actual outputs value in the datasets, $\overline{y}^*$ denotes the expected mean-value, and $\overline{y}$ show the actual average result.

3.4 Multi-objective model optimisation

3.4.1 Objective-function model establishment

The representation-capacity of compressive strength, flexural strength, as well as early age shrinkage were the well-understood FA-RF model. Furthermore, Equation (9) delivered the polynomial-equation as the cost-objective-equation for the activator.

$$\begin{aligned}\mathrm{Cost}\left(¥/\mathrm{m}^3\right) = {} & C_c Q_c + C_f Q_f + C_{MgO} Q_{MgO} + C_{CaO} Q_{CaO} \\ & + C_{fiber} Q_{fiber} + C_s Q_s + C_{st} Q_{st} + C_{sp} Q_{sp}\end{aligned} \tag{9}$$

In Equation (9), Q_f, Q_c, Q_{MgO}, Q_{CaO}, Q_{fiber}, Q_s, Q_{st}, Q_{sp} represented the amount (kg/m^3) of flyash, cement, MgO, CaO, fiber, sand, stone, superplasticizer, respectively, where C represented the unit each material price of TSWS mixtures, as shown in Table 3.

Table 3 Cost per unit of each material of TSWS.

Variables	Notation	Unit weight (kg/m^3)	Unit price (¥/ton)
cement	C_c	3060	600
flyash	C_f	2370	338
MgO	C_{MgO}	2360	2400
CaO	C_{CaO}	2570	1200
fiber	C_{fiber}	910	25000
sand	C_s	2628	194
stone	C_{st}	2678	120
superplasticizer	C_{sp}	1050	2516

3.4.2 Constraints

The constraints of input parameters (materials, volume, and ratio limitations) were set for MOO functions. The volume of the concrete material V_m is restricted as shown in equation (10), where U stands for the density of each material. The correlation between different raw materials was established by adjusting the proportion of each material to find the optimal TSWS concrete mix ratio, as summarized in Table 4.

$$V_m = \frac{Q_c}{U_c} + \frac{Q_f}{U_f} + \frac{Q_{MgO}}{U_{MgO}} + \frac{Q_{CaO}}{U_{CaO}} + \frac{Q_{fiber}}{U_{fiber}} + \frac{Q_s}{U_s} + \frac{Q_{st}}{U_{st}} + \frac{Q_{sp}}{U_{sp}} \tag{10}$$

Tab 4 The constraints input variables

Variables	Expressions	Upper limit (kg/m^3)	Lower limit (kg/m^3)
cement	Q_c	260	260
flyash	Q_f	125	125
MgO	Q_{MgO}	2.6	12
CaO	Q_{CaO}	18.2	36
fiber	Q_{fiber}	0.6	1.0
sand	Q_s	766	766
stone	Q_{st}	1078	1078
superplasticizer	Q_{sp}	7.1	7.1

3.4.3 MOFA-RF model development

The MOFA-RF model is established by blending three output variables (i.e. compressive strength, flexural strength, early age shrinkage) and a cost-oriented objective function. To tackle the multi-objective-optimization problem, numerous approaches were available, weighted-sum approach, complex approach, global-standard approach, as well as goal-programming. Out of these methods, the Weighted-Sum Method is the most commonly employed because of its ease of use. Weighted-sum method systematically changed the weights, uniquely determining different optimal solutions for each single objective optimization, and the set of these solutions approximately represent the Pareto frontier. This technique has been utilized to create a collection of multi-goal optimization procedures, including Multi-

Objective Optimization Algorithm and Multi-Objective Cuckoo Search. As so, weighted-sum was employed in this study, with function *F* expressed as follows:

$$F=\sum_{k=1}^{k}w_k f_k,\sum_{k=1}^{k}w_k=1,\quad w_k=\frac{p_k}{K} \tag{11}$$

where f_k represents the objective functions, w_k represents the weight, and p_k represents the uniformly distributed random-value (from 0 to 1). In this research, the relationship between three output variables, compressive strength (CS), flexural strength (FS), early age shrinkage (EAS) and a cost objective functions, and the cost objective function was determined through two three-objective functions as follows:

$$\begin{aligned} F_1 &= w_1\ \mathrm{CS}+w_2\ \mathrm{EAS}+w_3\ \mathrm{cost} \\ &= w_1\ \mathrm{FS}+w_2\ \mathrm{EAS}+w_3\ \mathrm{cost} \end{aligned} \tag{12}$$

$$\sum_{k=1}^{3}w_k=1 \tag{13}$$

The Non-dominated Solutions that Pareto Front can offer makes it a commonly used technique for Multi-objective Optimization[56]. It being supposed that there is no x，which is an element of set Z with feasible solutions and x* being one of the Pareto points, that satisfies:

$$f_k(x)\le f_k(x^*),\ for\quad k=1,2,3,...,\mathrm{t}\ and \tag{14}$$

$$f_k(x)<f_k(x^*),\ \ for\ atleast\ one\ k \tag{15}$$

For any x, if $f(x^*)$ is greater than $f(x)$, then the Pareto optimal solution x* can be obtained. Pareto frontier consists of multiple Pareto points as illustrated in Fig. 8.

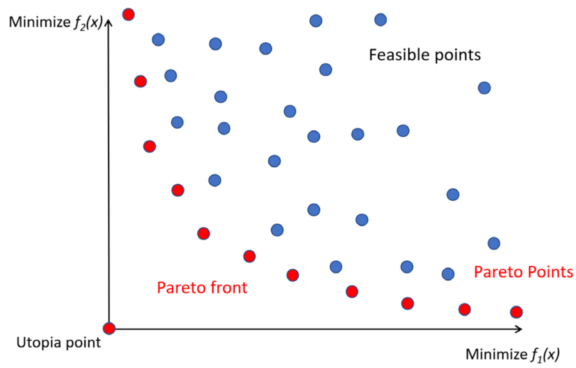

Fig. 8 Pareto front and feasible points.

3.4.4 Decision-making establishment for MOO model

Pareto frontier could be leveraged to tackle the MOO problem, but the optimal mixture proportion at the peak may not be the most suitable choice for algorithm decision-making. Subsequently, this model proposed the Technique of Preference by Similarity to an Ideal Solution (TOPSIS). TOPSIS concurrently selects the solution which is the furthest from the negative ideal point (di-) and the nearest to the positive ideal point (di+). The di- and di+ were the worst and best values of the objective function, respectively as follows:

$$d_{\mathrm{i+}} = \sqrt{\sum_{j=1}^{n}\left(F_{ij} - F_j^{\mathrm{ideal}}\right)^2} \tag{15}$$

$$d_{\mathrm{i-}} = \sqrt{\sum_{j=1}^{n}\left(F_{\mathrm{ij}} - F_j^{non-\mathrm{ideal}}\right)^2} \tag{16}$$

$$C_{\mathrm{i}} = \frac{d_{\mathrm{i-}}}{d_{\mathrm{i+}} + d_{\mathrm{i-}}} \tag{17}$$

where n is the sum of objective number and i denotes the ith Pareto point; F_j^{ideal} and $F_j^{non-\mathrm{ideal}}$ denote the ideal and non-ideal values of the jth objective, respectively.

4. Results and discussion

4.1 Laboratory experiment result

Figure 9 illustrates the correlation between different input variables (EA content, CaO-MgO ratio and fiber content) and the mechanical performance (CS, FA and EAS) of TSWS experimentally. The addition of expansive agent and CaO had negative effects on the CS and FS. CaO reduced mechanical performances at 6.0%, which was less than EA (-12.6%). Meanwhile, the fiber had a positive effect on the CS and FS, but the influence was relatively small (1.8%). However, expansive agent and CaO imposed positive consequences on EAS by volume expansive. The effect of CaO on EAS (9.4%) was less than that of the expansive agent (28.0%), however, the addition of fibers had a minor yet positive influence on EAS (4.4%).

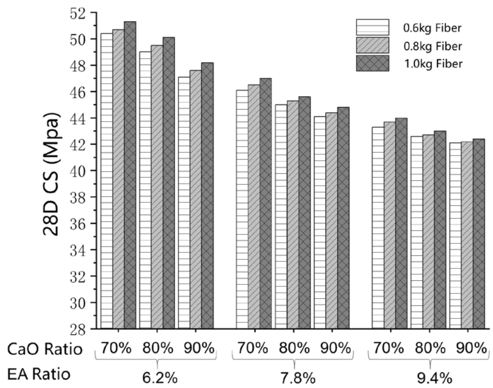

(a)

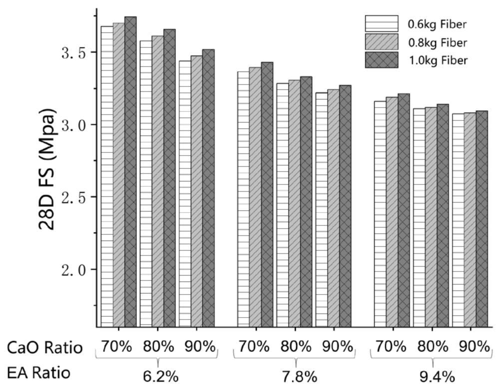

(b)

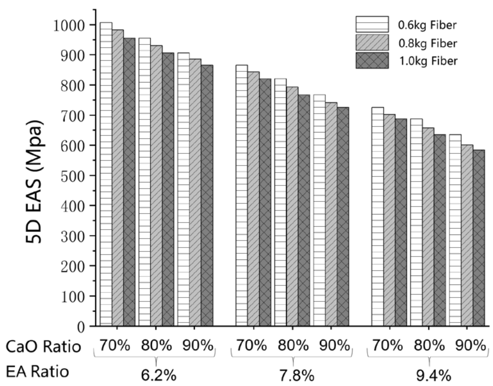

(c)

Fig. 9 The outputs (CS (a) FS (b) EAS (c)) for TSWS mixtures including different expansion agent, CaO-MgO ratio and fiber content.

4.2 Modelling results

4.2.1 Results of hyperparameter tuning

NumTree and minNumLeaf were optimized and adjusted by FA as well as 10-fold CV. The 10-fold CV generated an optimized RMSE displayed in Fig. 10. On FS, CS and EAS datasets, the optimized RMSE was respectively spotted at the 4th, 5th and 4th folds. Figure 11 illustrates the respective RMSE of the iterative samples. Results showed that 8, 49, and 43 iterations were obligated to acquire the optimized results, which confirmed the efficiency and validity of the FA model for optimizing hyperparameters. Finally, the fixed hyperparameters of constructed Random Forest models was as follows: CS (numTree=7, minNumLeaf=1), FS (numTree=14, minNumLeaf=1), EAS (numTree=14, minNumLeaf=1).

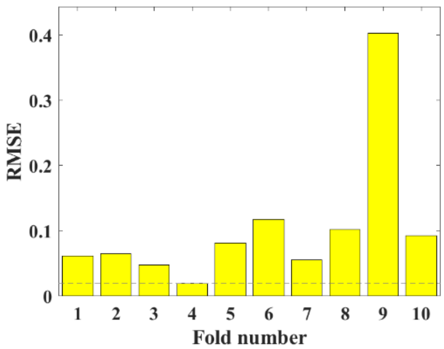

(a)

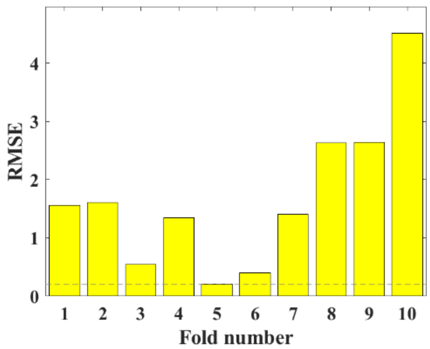

(b)

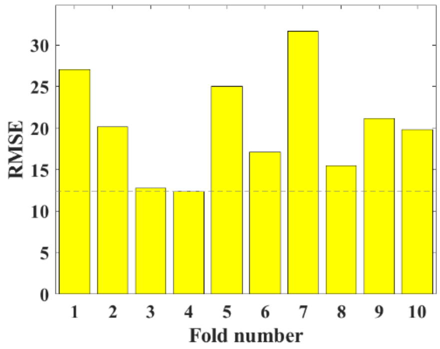

Fig. 10 RMSE of 10-fold CV for on the (a) FS (b) CS (c) EAS dataset.

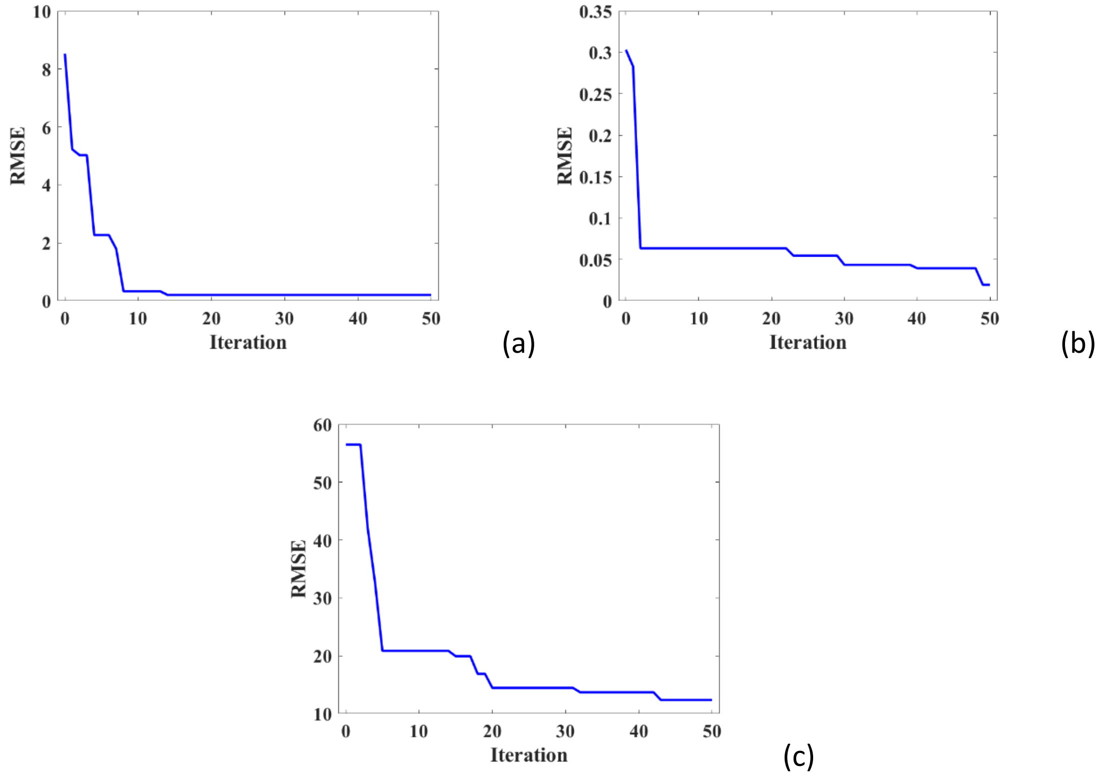

Fig. 11 RMSE iteration in the optimal fold of datasets.

4.2.2 Performance of FA-RF model

Fig. 12 illustrated the prediction performance results of FA-RF model both on the test-training set. The distance between the solid black line and the dots was in positive to the error between predicted and actual values. Most points stayed close to the diagonal line, pointing to the adequacy of the predictions rendered by the three-constructed FA-RF models on the datasets. Table 5 summarised four evaluation evaluation indicators (RMSE, R, MAPE and MAE) for FA-RF model on the test set when predicting the CS, FS, and EAS. The R values of 0.9997, 0.9995 and 0.9787 demonstrated that there was negligible discrepancy between the actual and predicted outcome. The MEA, RMSE and MAPE values were also relatively low, substantiating the veracity of the predictive models. The R or RMSE scores of the test set and training set were fairly similar, thus greatly reducing the potential risks of underfitting or overfitting.

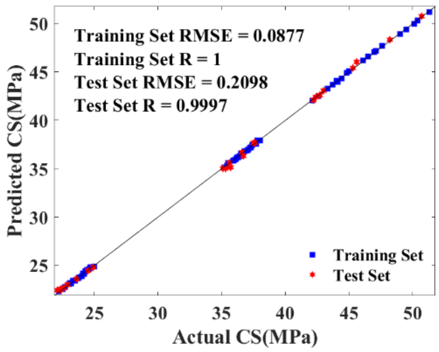

(a)

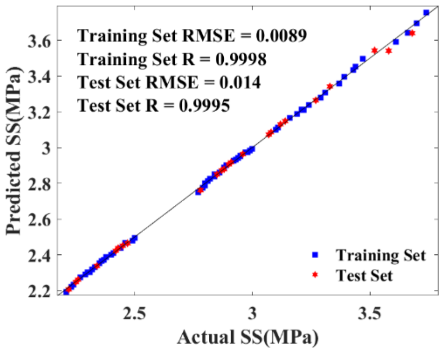

(b)

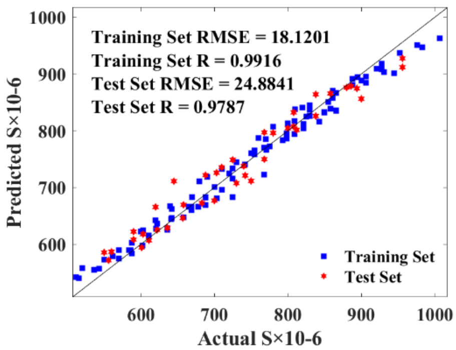

(c)

Fig. 12 Actual compared to predicted values for (a) CS (b) FS (c) EAS.

Table 5 Evaluation index of training set.

Test category	Evaluation index			
	R	RMSE	MAE	MAPE
CS	0.9997	0.210	0.154	0.005
FS	0.9995	0. 014	0.009	0.003
EAS$\times 10^{-6}$	0.9787	24.88×10^{-6}	24.46×10^{-6}	0.029

4.2.3 TSWS mixture optimisation

The purpose of this study was to minimize EAS of concrete and maximize 28-day CS and FS while minimizing cost after establishing three FA-RF models. The Pareto front of the tri-objective (EAS, cost, and CS) optimized design, depicted in Fig. 13, was achieved due to the CS, FS and EAS are the output variables and both the CS and the FS were mechanical performances with correlation. Altogether, non-dominated Pareto-points at 100 were produced along the Pareto-front, providing a suitable cubic relationship between CS, EAS and cost, exhibiting that the MOFA-RF models was effective. In order to enhance the mechanical performance of TSWS (CS, FS and EAS), it is necessary to increase the cost, considering that a greater cement content leads to a greater cement cost and the related mechanical strength is higher than that of both sands and water.

Out of 100 non-inferior solutions, Point A, B, C, and D can be regarded as special points in terms of MOO and single-objective optimization configurations, for, they all achieved highest TOPSIS, lowest cost, minimum EAS, and maximum CS, respectively. In Fig. 13, the 28-day CS reached the highest values at 51.8 MPa (point D) while EAS reached 998×10^{-6} due to parameter of expansibility admixture was reduced. Point C represented the lowest EAS (715×10^{-6}), the CS was reduced to 40.5MPa due to the negative influence of expansive agent. Meanwhile, at Point B, the lowest cost (552.8 ¥/m^3) was observed, though with the sizable decrease on the mechanical property (42.3 MPa). With respect to TOPSIS, Point A was identified as the optimal solution, revealing the balance between the three goals, leading to the peak TOPSIS result of 1 with 47.1 MPa CS, 787×10^{-6} EAS, and a cost of 560.8 ¥/m^3.

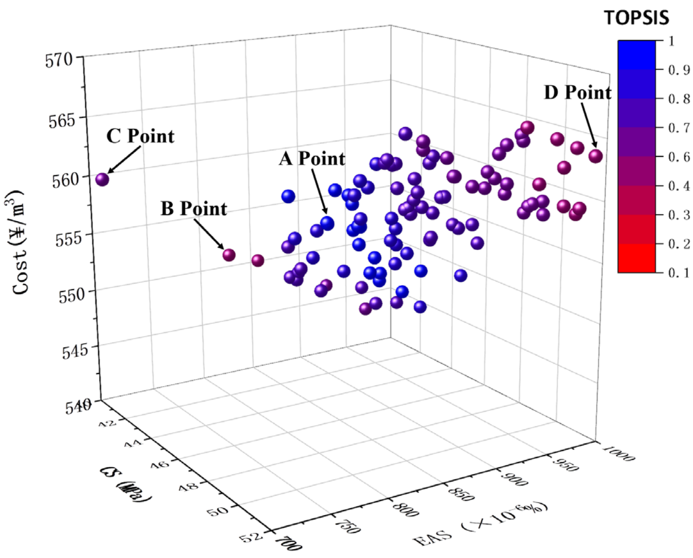

Fig. 13 Pareto fronts of CS, EAS and cost.

5. Conclusions

The study assessed the impact of CaO, MgO, and fiber content on compressive strength, flexural strength, and early-age shrinkage in tunnel side wall structures through shrinkage and compressive tests. Subsequently, effective Pareto-fronts were obtained through proposing the MOFA-RF model. The main conclusions are as follows:

(1) Expansion agent content decreased mechanical properties by 6%-12.6% yet significantly reduced EAS by 9.4%-28%. This effect is linked to the expansion of CaO and MgO crystals during cement hydration.

(2) An optimized TSWS mix ratio (Q_c: Q_f: Q_{MgO}: Q_{CaO}: Q_{fiber}: Q_s: Q_{st}: Q_{sp} = 260: 125: 31.8: 6.4: 0.6: 766: 1078: 149: 7.1 kg/m^3) was established to balance mechanical properties, EAS, and cost.

(3) The FA-RF models proved efficient, evidenced by low RMSE values (CS: 0.21, FS: 0.014, EAS: 24.88) and high correlation coefficients (CS: 0.9999, FS: 0.9997, EAS: 0.9787). However, these models are primarily suited to laboratory data, and adjustments are necessary for field application due to discrepancies between laboratory and field results.

(4) The MOFA-RF-based tri-objective optimization models effectively generated Pareto fronts, offering viable alternatives for decision-making. The TOPSIS method identified Point A as the optimal solution, featuring a CS of 47.1 MPa, an EAS of 787×10^{-6}, and a cost of 560.8 ¥/m^3.

Given the impact of limited data on ML model performance, expanding databases and advancing model technology are essential steps to achieve superior accuracy, efficiency, and wider applicability.

5. Acknowledgements

The project is supported by Hunan Provincial Key Laboratory of Structures for Wind Resistance and Vibration Control, Hunan University of Science and Technology. The project is also funded by the Key R&D Project of Hunan Province Intelligent Disaster Prevention and Mitigation and Ecological Restoration in Civil Engineering (2020SK2109).

Appendix

Table 6 Mechanical performance for TSWS composites(MPa)

Cemen	FA	MgO	CaO	Fibe	Sand	CA	Wate	SP	Age	FS	CS
260	125	2.6	23.4	0.6	766	1078	149	7.1	0.54	2.41	24.1
260	125	2.6	23.4	0.8	766	1078	149	7.1	0.54	2.42	24.2
260	125	2.6	23.4	1	766	1078	149	7.1	0.54	2.43	24.3
260	125	5.2	20.8	0.6	766	1078	149	7.1	0.54	2.44	24.4
260	125	5.2	20.8	0.8	766	1078	149	7.1	0.54	2.45	24.5
260	125	5.2	20.8	1	766	1078	149	7.1	0.54	2.46	24.6
260	125	7.8	18.2	0.6	766	1078	149	7.1	0.54	2.47	24.7
260	125	7.8	18.2	0.8	766	1078	149	7.1	0.54	2.49	24.9
260	125	7.8	18.2	1	766	1078	149	7.1	0.54	2.50	25
260	125	3.3	29.7	0.6	766	1078	151	7.1	0.54	2.31	23.1
260	125	3.3	29.7	0.8	766	1078	151	7.1	0.54	2.32	23.2
260	125	3.3	29.7	1	766	1078	151	7.1	0.54	2.33	23.3
260	125	6.6	26.4	0.6	766	1078	151	7.1	0.54	2.34	23.4
260	125	6.6	26.4	0.8	766	1078	151	7.1	0.54	2.35	23.5
260	125	6.6	26.4	1	766	1078	151	7.1	0.54	2.36	23.6
260	125	9.9	23.1	0.6	766	1078	151	7.1	0.54	2.37	23.7
260	125	9.9	23.1	0.8	766	1078	151	7.1	0.54	2.38	23.8
260	125	9.9	23.1	1	766	1078	151	7.1	0.54	2.40	24
260	125	4	36	0.6	766	1078	154	7.1	0.54	2.21	22.1
260	125	4	36	0.8	766	1078	154	7.1	0.54	2.22	22.2
260	125	4	36	1	766	1078	154	7.1	0.54	2.23	22.3
260	125	8	32	0.6	766	1078	154	7.1	0.54	2.24	22.4
260	125	8	32	0.8	766	1078	154	7.1	0.54	2.25	22.5
260	125	8	32	1	766	1078	154	7.1	0.54	2.26	22.6
260	125	12	28	0.6	766	1078	154	7.1	0.54	2.27	22.7
260	125	12	28	0.8	766	1078	154	7.1	0.54	2.29	22.9
260	125	12	28	1	766	1078	154	7.1	0.54	2.3	23
260	125	2.6	23.4	0.6	766	1078	149	7.1	1.25	2.93	37.1
260	125	2.6	23.4	0.8	766	1078	149	7.1	1.25	2.94	37.2
260	125	2.6	23.4	1	766	1078	149	7.1	1.25	2.95	37.3
260	125	5.2	20.8	0.6	766	1078	149	7.1	1.25	2.95	37.4
260	125	5.2	20.8	0.8	766	1078	149	7.1	1.25	2.96	37.5
260	125	5.2	20.8	1	766	1078	149	7.1	1.25	2.97	37.6
260	125	7.8	18.2	0.6	766	1078	149	7.1	1.25	2.98	37.7
260	125	7.8	18.2	0.8	766	1078	149	7.1	1.25	2.99	37.8

260	125	7.8	18.2	1	766	1078	149	7.1	1.25	3.00	38
260	125	3.3	29.7	0.6	766	1078	151	7.1	1.25	2.85	36.1
260	125	3.3	29.7	0.8	766	1078	151	7.1	1.25	2.86	36.2
260	125	3.3	29.7	1	766	1078	151	7.1	1.25	2.87	36.3
260	125	6.6	26.4	0.6	766	1078	151	7.1	1.25	2.88	36.4
260	125	6.6	26.4	0.8	766	1078	151	7.1	1.25	2.88	36.5
260	125	6.6	26.4	1	766	1078	151	7.1	1.25	2.89	36.6
260	125	9.9	23.1	0.6	766	1078	151	7.1	1.25	2.90	36.7
260	125	9.9	23.1	0.8	766	1078	151	7.1	1.25	2.91	36.8
260	125	9.9	23.1	1	766	1078	151	7.1	1.25	2.92	37
260	125	4	36	0.6	766	1078	154	7.1	1.25	2.77	35.1
260	125	4	36	0.8	766	1078	154	7.1	1.25	2.78	35.2
260	125	4	36	1	766	1078	154	7.1	1.25	2.79	35.3
260	125	8	32	0.6	766	1078	154	7.1	1.25	2.80	35.4
260	125	8	32	0.8	766	1078	154	7.1	1.25	2.80	35.5
260	125	8	32	1	766	1078	154	7.1	1.25	2.81	35.6
260	125	12	28	0.6	766	1078	154	7.1	1.25	2.82	35.7
260	125	12	28	0.8	766	1078	154	7.1	1.25	2.84	35.9
260	125	12	28	1	766	1078	154	7.1	1.25	2.84	36
260	125	2.6	23.4	0.6	766	1078	149	7.1	5	3.44	47.1
260	125	2.6	23.4	0.8	766	1078	149	7.1	5	3.47	47.6
260	125	2.6	23.4	1	766	1078	149	7.1	5	3.52	48.2
260	125	5.2	20.8	0.6	766	1078	149	7.1	5	3.58	49
260	125	5.2	20.8	0.8	766	1078	149	7.1	5	3.61	49.5
260	125	5.2	20.8	1	766	1078	149	7.1	5	3.66	50.1
260	125	7.8	18.2	0.6	766	1078	149	7.1	5	3.68	50.4
260	125	7.8	18.2	0.8	766	1078	149	7.1	5	3.70	50.7
260	125	7.8	18.2	1	766	1078	149	7.1	5	3.74	51.3
260	125	3.3	29.7	0.6	766	1078	151	7.1	5	3.22	44.1
260	125	3.3	29.7	0.8	766	1078	151	7.1	5	3.24	44.4
260	125	3.3	29.7	1	766	1078	151	7.1	5	3.27	44.8
260	125	6.6	26.4	0.6	766	1078	151	7.1	5	3.29	45
260	125	6.6	26.4	0.8	766	1078	151	7.1	5	3.31	45.3
260	125	6.6	26.4	1	766	1078	151	7.1	5	3.33	45.6
260	125	9.9	23.1	0.6	766	1078	151	7.1	5	3.37	46.1
260	125	9.9	23.1	0.8	766	1078	151	7.1	5	3.39	46.5
260	125	9.9	23.1	1	766	1078	151	7.1	5	3.43	47
260	125	4	36	0.6	766	1078	154	7.1	5	3.07	42.1
260	125	4	36	0.8	766	1078	154	7.1	5	3.08	42.2
260	125	4	36	1	766	1078	154	7.1	5	3.10	42.4
260	125	8	32	0.6	766	1078	154	7.1	5	3.11	42.6

260	125	8	32	0.8	766	1078	154	7.1	5	3.12	42.7
260	125	8	32	1	766	1078	154	7.1	5	3.14	43
260	125	12	28	0.6	766	1078	154	7.1	5	3.16	43.3
260	125	12	28	0.8	766	1078	154	7.1	5	3.19	43.7
260	125	12	28	1	766	1078	154	7.1	5	3.21	44

Table 7 Early age shrinkage for TSWS composites($\times 10^{-6}$)

Cement	FA	MgO	CaO	Fiber	Sand	CA	Water	SP	Age	EAS
260	125	2.6	23.4	0.6	766	1078	149	7.1	1	800
260	125	2.6	23.4	0.8	766	1078	149	7.1	1	770
260	125	2.6	23.4	1	766	1078	149	7.1	1	760
260	125	5.2	20.8	0.6	766	1078	149	7.1	1	825
260	125	5.2	20.8	0.8	766	1078	149	7.1	1	800
260	125	5.2	20.8	1	766	1078	149	7.1	1	780
260	125	7.8	18.2	0.6	766	1078	149	7.1	1	861
260	125	7.8	18.2	0.8	766	1078	149	7.1	1	830
260	125	7.8	18.2	1	766	1078	149	7.1	1	810
260	125	3.3	29.7	0.6	766	1078	151	7.1	1	670
260	125	3.3	29.7	0.8	766	1078	151	7.1	1	640
260	125	3.3	29.7	1	766	1078	151	7.1	1	620
260	125	6.6	26.4	0.6	766	1078	151	7.1	1	710
260	125	6.6	26.4	0.8	766	1078	151	7.1	1	680
260	125	6.6	26.4	1	766	1078	151	7.1	1	645
260	125	9.9	23.1	0.6	766	1078	151	7.1	1	740
260	125	9.9	23.1	0.8	766	1078	151	7.1	1	720
260	125	9.9	23.1	1	766	1078	151	7.1	1	690
260	125	4	36	0.6	766	1078	154	7.1	1	550
260	125	4	36	0.8	766	1078	154	7.1	1	520
260	125	4	36	1	766	1078	154	7.1	1	512
260	125	8	32	0.6	766	1078	154	7.1	1	590
260	125	8	32	0.8	766	1078	154	7.1	1	560
260	125	8	32	1	766	1078	154	7.1	1	550
260	125	12	28	0.6	766	1078	154	7.1	1	620
260	125	12	28	0.8	766	1078	154	7.1	1	600
260	125	12	28	1	766	1078	154	7.1	1	590
260	125	2.6	23.4	0.6	766	1078	149	7.1	2	808
260	125	2.6	23.4	0.8	766	1078	149	7.1	2	780
260	125	2.6	23.4	1	766	1078	149	7.1	2	768
260	125	5.2	20.8	0.6	766	1078	149	7.1	2	858
260	125	5.2	20.8	0.8	766	1078	149	7.1	2	830
260	125	5.2	20.8	1	766	1078	149	7.1	2	808

260	125	7.8	18.2	0.6	766	1078	149	7.1	2	894
260	125	7.8	18.2	0.8	766	1078	149	7.1	2	880
260	125	7.8	18.2	1	766	1078	149	7.1	2	858
260	125	3.3	29.7	0.6	766	1078	151	7.1	2	688
260	125	3.3	29.7	0.8	766	1078	151	7.1	2	665
260	125	3.3	29.7	1	766	1078	151	7.1	2	642
260	125	6.6	26.4	0.6	766	1078	151	7.1	2	725
260	125	6.6	26.4	0.8	766	1078	151	7.1	2	703
260	125	6.6	26.4	1	766	1078	151	7.1	2	688
260	125	9.9	23.1	0.6	766	1078	151	7.1	2	768
260	125	9.9	23.1	0.8	766	1078	151	7.1	2	742
260	125	9.9	23.1	1	766	1078	151	7.1	2	725
260	125	4	36	0.6	766	1078	154	7.1	2	570
260	125	4	36	0.8	766	1078	154	7.1	2	543
260	125	4	36	1	766	1078	154	7.1	2	516
260	125	8	32	0.6	766	1078	154	7.1	2	603
260	125	8	32	0.8	766	1078	154	7.1	2	586
260	125	8	32	1	766	1078	154	7.1	2	570
260	125	12	28	0.6	766	1078	154	7.1	2	642
260	125	12	28	0.8	766	1078	154	7.1	2	621
260	125	12	28	1	766	1078	154	7.1	2	603
260	125	2.6	23.4	0.6	766	1078	149	7.1	3	850
260	125	2.6	23.4	0.8	766	1078	149	7.1	3	830
260	125	2.6	23.4	1	766	1078	149	7.1	3	809
260	125	5.2	20.8	0.6	766	1078	149	7.1	3	900
260	125	5.2	20.8	0.8	766	1078	149	7.1	3	855
260	125	5.2	20.8	1	766	1078	149	7.1	3	820
260	125	7.8	18.2	0.6	766	1078	149	7.1	3	945
260	125	7.8	18.2	0.8	766	1078	149	7.1	3	921
260	125	7.8	18.2	1	766	1078	149	7.1	3	900
260	125	3.3	29.7	0.6	766	1078	151	7.1	3	710
260	125	3.3	29.7	0.8	766	1078	151	7.1	3	683
260	125	3.3	29.7	1	766	1078	151	7.1	3	669
260	125	6.6	26.4	0.6	766	1078	151	7.1	3	755
260	125	6.6	26.4	0.8	766	1078	151	7.1	3	730
260	125	6.6	26.4	1	766	1078	151	7.1	3	710
260	125	9.9	23.1	0.6	766	1078	151	7.1	3	809
260	125	9.9	23.1	0.8	766	1078	151	7.1	3	775
260	125	9.9	23.1	1	766	1078	151	7.1	3	755
260	125	4	36	0.6	766	1078	154	7.1	3	588
260	125	4	36	0.8	766	1078	154	7.1	3	556
260	125	4	36	1	766	1078	154	7.1	3	536

260	125	8	32	0.6	766	1078	154	7.1	3	622
260	125	8	32	0.8	766	1078	154	7.1	3	602
260	125	8	32	1	766	1078	154	7.1	3	588
260	125	12	28	0.6	766	1078	154	7.1	3	669
260	125	12	28	0.8	766	1078	154	7.1	3	641
260	125	12	28	1	766	1078	154	7.1	3	622
260	125	2.6	23.4	0.6	766	1078	149	7.1	4	888
260	125	2.6	23.4	0.8	766	1078	149	7.1	4	861
260	125	2.6	23.4	1	766	1078	149	7.1	4	838
260	125	5.2	20.8	0.6	766	1078	149	7.1	4	928
260	125	5.2	20.8	0.8	766	1078	149	7.1	4	895
260	125	5.2	20.8	1	766	1078	149	7.1	4	888
260	125	7.8	18.2	0.6	766	1078	149	7.1	4	976
260	125	7.8	18.2	0.8	766	1078	149	7.1	4	952
260	125	7.8	18.2	1	766	1078	149	7.1	4	928
260	125	3.3	29.7	0.6	766	1078	151	7.1	4	750
260	125	3.3	29.7	0.8	766	1078	151	7.1	4	730
260	125	3.3	29.7	1	766	1078	151	7.1	4	700
260	125	6.6	26.4	0.6	766	1078	151	7.1	4	798
260	125	6.6	26.4	0.8	766	1078	151	7.1	4	771
260	125	6.6	26.4	1	766	1078	151	7.1	4	750
260	125	9.9	23.1	0.6	766	1078	151	7.1	4	838
260	125	9.9	23.1	0.8	766	1078	151	7.1	4	812
260	125	9.9	23.1	1	766	1078	151	7.1	4	798
260	125	4	36	0.6	766	1078	154	7.1	4	611
260	125	4	36	0.8	766	1078	154	7.1	4	586
260	125	4	36	1	766	1078	154	7.1	4	562
260	125	8	32	0.6	766	1078	154	7.1	4	658
260	125	8	32	0.8	766	1078	154	7.1	4	636
260	125	8	32	1	766	1078	154	7.1	4	611
260	125	12	28	0.6	766	1078	154	7.1	4	700
260	125	12	28	0.8	766	1078	154	7.1	4	678
260	125	12	28	1	766	1078	154	7.1	4	658
260	125	2.6	23.4	0.6	766	1078	149	7.1	5	906
260	125	2.6	23.4	0.8	766	1078	149	7.1	5	886
260	125	2.6	23.4	1	766	1078	149	7.1	5	866
260	125	5.2	20.8	0.6	766	1078	149	7.1	5	956
260	125	5.2	20.8	0.8	766	1078	149	7.1	5	931
260	125	5.2	20.8	1	766	1078	149	7.1	5	906
260	125	7.8	18.2	0.6	766	1078	149	7.1	5	1007
260	125	7.8	18.2	0.8	766	1078	149	7.1	5	983
260	125	7.8	18.2	1	766	1078	149	7.1	5	956

260	125	3.3	29.7	0.6	766	1078	151	7.1	5	768
260	125	3.3	29.7	0.8	766	1078	151	7.1	5	742
260	125	3.3	29.7	1	766	1078	151	7.1	5	725
260	125	6.6	26.4	0.6	766	1078	151	7.1	5	821
260	125	6.6	26.4	0.8	766	1078	151	7.1	5	793
260	125	6.6	26.4	1	766	1078	151	7.1	5	768
260	125	9.9	23.1	0.6	766	1078	151	7.1	5	866
260	125	9.9	23.1	0.8	766	1078	151	7.1	5	843
260	125	9.9	23.1	1	766	1078	151	7.1	5	821
260	125	4	36	0.6	766	1078	154	7.1	5	636
260	125	4	36	0.8	766	1078	154	7.1	5	601
260	125	4	36	1	766	1078	154	7.1	5	584
260	125	8	32	0.6	766	1078	154	7.1	5	688
260	125	8	32	0.8	766	1078	154	7.1	5	657
260	125	8	32	1	766	1078	154	7.1	5	636
260	125	12	28	0.6	766	1078	154	7.1	5	725
260	125	12	28	0.8	766	1078	154	7.1	5	703
260	125	12	28	1	766	1078	154	7.1	5	688

References

1. Zhao, H.T., et al., *Effects of reinforcement on autogenous deformation of early-age concrete containing CaO-based expansion agent.* Construction and Building Materials, 2022. **320**.
2. He, H., et al., *The influence of pipe-jacking tunneling on deformation of existing tunnels in soft soils and the effectiveness of protection measures.* Transportation Geotechnics, 2023. **42**: p. 101061 doi: https://doi.org/10.1016/j.trgeo.2023.101061.
3. Hu, D., et al., *Experiment and Application of NATM Tunnel Deformation Monitoring Based on 3D Laser Scanning.* Structural Control and Health Monitoring, 2023. **2023**: p. 3341788 doi: 10.1155/2023/3341788.
4. Yang, Y., et al., *Research Progress of SHM System for Super High-Rise Buildings Based on Wireless Sensor Network and Cloud Platform.* Remote Sensing, 2023. **15**(6): p. 1473 https://doi.org/10.3390/rs15061473.
5. Zhang, Z.B., et al. *Effect of Amount on Expansion Property of MgO-type Expansive Agent Used in Cement-based Materials*. in *International Symposium on Chemical Engineering and Materials Properties (ISCEMP 2011)*. 2011. Shenyang, PEOPLES R CHINA.
6. Shen, D.J., et al., *Restrained cracking failure behavior of concrete containing MgO compound expansive agent under adiabatic condition at early age.* Cement & Concrete Composites, 2023. **135**.

7. Pang, B., et al., *Inner superhydrophobic materials based on waste fly ash: Microstructural morphology of microetching effects.* Composites Part B: Engineering, 2024. **268**: p. 111089 doi: https://doi.org/10.1016/j.compositesb.2023.111089.
8. Shi, M., et al., *Ensemble regression based on polynomial regression-based decision tree and its application in the in-situ data of tunnel boring machine.* Mechanical Systems and Signal Processing, 2023. **188**: p. 110022 doi: https://doi.org/10.1016/j.ymssp.2022.110022.
9. Saradar, A., et al., *Restrained Shrinkage Cracking of Fiber-Reinforced High-Strength Concrete.* Fibers, 2018. **6**(1).
10. Liu, C., et al., *The role of TBM asymmetric tail-grouting on surface settlement in coarse-grained soils of urban area: Field tests and FEA modelling.* Tunnelling and Underground Space Technology, 2021. **111**: p. 103857 doi: https://doi.org/10.1016/j.tust.2021.103857.
11. Wang, M., X. Yang, and W. Wang, *Establishing a 3D aggregates database from X-ray CT scans of bulk concrete.* Construction and Building Materials, 2022. **315**: p. 125740 doi: https://doi.org/10.1016/j.conbuildmat.2021.125740.
12. Zhang, G.B., et al., *Properties of sustainable self-compacting concrete containing activated jute fiber and waste mineral powders.* JOURNAL OF MATERIALS RESEARCH AND TECHNOLOGY-JMR&T, 2022. **19**: p. 1740-1758.
13. Zhang, W., et al. *Flexural behavior of SFRC-NC composite beams: An experimental and numerical analytical study*. in *Structures*. 2024. Elsevier.
14. Long, X., et al., *Machine learning method to predict dynamic compressive response of concrete-like material at high strain rates.* Defence Technology, 2023. **23**: p. 100-111 doi: https://doi.org/10.1016/j.dt.2022.02.003.
15. Pan, Z.F., et al., *Effect of expansive agents on the workability, crack resistance and durability of shrinkage-compensating concrete with low contents of fibers.* Construction and Building Materials, 2020. **259**.
16. Yang, Y., B. Lin, and W. Zhang, *Experimental and numerical investigation of an arch–beam joint for an arch bridge.* Archives of Civil and Mechanical Engineering, 2023. **23**(2): p. 101 doi: 10.1007/s43452-023-00645-3.
17. Huang, H., et al., *Seismic behavior of a friction-type artificial plastic hinge for the precast beam–column connection.* Archives of Civil and Mechanical Engineering, 2022. **22**(4): p. 201 doi: 10.1007/s43452-022-00526-1.
18. Memon, I.A., et al., *Influence of Fibre Length on the Behaviour of Polypropylene Fibre Reinforced Cement Concrete.* Civil Engineering Journal-Tehran, 2018. **4**(9): p. 2124-2131.
19. Yao, Y., et al. *Cyclic performance of novel composite beam-to-column connections with reduced beam section fuse elements*. in *Structures*. 2023. Elsevier.
20. Yang, Y., et al., *Damage identification of frame structure based on approximate Metropolis–Hastings algorithm and probability density evolution method.*

International Journal of Structural Stability and Dynamics, 2022. **22**(03n04): p. 2240014 https://doi.org/10.1142/S0219455422400144.

21. Qin, Y., et al., *Experimental study of compressive behavior of polypropylene-fiber-reinforced and polypropylene-fiber-fabric-reinforced concrete.* Construction and Building Materials, 2019. **194**: p. 216-225.
22. Mazzoli, A., S. Monosi, and E.S. Plescia, *Evaluation of the early-age-shrinkage of Fiber Reinforced Concrete (FRC) using image analysis methods.* Construction and Building Materials, 2015. **101**: p. 596-601.
23. Gong, J.Q., W. Zeng, and W.J. Zhang, *Influence of shrinkage-reducing agent and polypropylene fiber on shrinkage of ceramsite concrete.* Construction and Building Materials, 2018. **159**: p. 155-163.
24. Zhang, J. and C. Zhang, *Using viscoelastic materials to mitigate earthquake-induced pounding between adjacent frames with unequal height considering soil-structure interactions.* Soil Dynamics and Earthquake Engineering, 2023. **172**: p. 107988 doi: https://doi.org/10.1016/j.soildyn.2023.107988.
25. Kassimi, F. and M.H. Khayat, *Shrinkage of high-performance fiber-reinforced concrete with adapted rheology.* Construction and Building Materials, 2020. **232**.
26. Jasiczak, J., P. Szymanski, and P. Nowotarski, *Computerised evaluation of the early age of shrinkage in concrete.* Automation in Construction, 2015. **49**: p. 40-50.
27. Chen, X., H.Q. Yang, and W.W. Li, *Factors analysis on autogenous volume deformation of MgO concrete and early thermal cracking evaluation.* Construction and Building Materials, 2016. **118**: p. 276-285.
28. Li, S.K., et al., *Mitigation on the autogenous shrinkage of ultra-high performance concrete via using MgO expansive agent.* Construction and Building Materials, 2021. **312**.
29. Sun, J.B., et al., *Mechanical Performance Prediction for Sustainable High-Strength Concrete Using Bio-Inspired Neural Network.* BUILDINGS, 2022. **12**(1).
30. Sun, J.B., et al., *Machine learning-aided design and prediction of cementitious composites containing graphite and slag powder.* JOURNAL OF BUILDING ENGINEERING, 2021. **43**.
31. Guo, J.N., et al., *Effect of calcium sulfoaluminate and MgO expansive agent on the mechanical strength and crack resistance of concrete.* Construction and Building Materials, 2021. **299**.
32. Li, H., et al., *Effect of CaO and MgO based expansive agent on deformation and mechanical properties of concrete-filled steel tubes.* Construction and Building Materials, 2020. **250**.
33. Ma, L., et al., *Pore structure, internal relative humidity, and fiber orientation of 3D printed concrete with polypropylene fiber and their relation with shrinkage.* Journal of Building Engineering, 2022. **61**.

34. Liu, T.G., et al., *Recycling of Materials for Pavement Dressing: Analytical Review.* Science & Technique, 2019. **18**(2): p. 104-112.
35. Liu, P., Z.Y. Chen, and M. Deng, *Regulating the Expansion Characteristics of Cementitious Materials Using Blended MgO-Type Expansive Agent.* Materials, 2019. **12**(6).
36. Li, M., et al., *Shrinkage crack inhibiting of cast in situ tunnel concrete by double regulation on temperature and deformation of concrete at early age.* Construction and Building Materials, 2020. **240**.
37. Li, C.Y., et al., *Shrinkage and Mechanical Properties of Self-Compacting SFRC With Calcium-Sulfoaluminate Expansive Agent.* Materials, 2020. **13**(3).
38. Sun, Y.T., et al., *Development of an Ensemble Intelligent Model for Assessing the Strength of Cemented Paste Backfill.* Advances in Civil Engineering, 2020. **2020**.
39. Sun, J.B., et al., *Multi-objective optimisation of a graphite-slag conductive composite applying a BAS-SVR based model.* Journal of Building Engineering, 2021. **44**.
40. Tang, Y., et al., *An experimental investigation and machine learning-based prediction for seismic performance of steel tubular column filled with recycled aggregate concrete.* Reviews on Advanced Materials Science, 2022. **61**(1): p. 849-872.
41. Zhang, G.B., et al., *Multi-objective optimisation design for GFRP tendon reinforced cemented soil.* CONSTRUCTION AND BUILDING MATERIALS, 2022. **320**.
42. Sun, J.B., et al., *Molecular interfacial properties and engineering performance of conductive fillers in cementitious composites.* JOURNAL OF MATERIALS RESEARCH AND TECHNOLOGY-JMR&T, 2022. **19**: p. 591-604.
43. Yao, X., et al., *AI-based performance prediction for 3D-printed concrete considering anisotropy and steam curing condition.* Construction and Building Materials, 2023. **375**: p. 130898.
44. Abedini, M. and C.W. Zhang, *Dynamic performance of concrete columns retro fi tted with FRP using segment pressure technique.* Composite Structures, 2021. **260**.
45. Tang, Y., et al., *Exploring temperature-resilient recycled aggregate concrete with waste rubber: An experimental and multi-objective optimization analysis.* Reviews on Advanced Materials Science, 2023. **62**(1): p. 20230347.
46. Zhang, J., et al., *Machine-learning-assisted shear strength prediction of reinforced concrete beams with and without stirrups.* Engineering with Computers, 2020: p. 1-15.
47. Sun, J., et al., *Mechanical properties prediction of lightweight coal gangue shotcrete.* Journal of Building Engineering, 2023. **80**: p. 108088.
48. Yang, Y., et al., *Fundamental mode shape estimation and element stiffness evaluation of girder bridges by using passing tractor-trailers.* Mechanical

Systems and Signal Processing, 2022. **169**: p. 108746 https://doi.org/10.1016/j.ymssp.2021.108746.

49. Yang, Y., et al., *Bridge bearing damage identification based on statistical moment change rate.* Mechanical Systems and Signal Processing, 2024. **206**: p. 110898.

50. Zhang, J.F., et al., *Mixture optimization for environmental, economical and mechanical objectives in silica fume concrete: A novel frame-work based on machine learning and a new meta-heuristic algorithm.* Resources Conservation and Recycling, 2021. **167**.

51. Feng, W., et al., *Prediction of thermo-mechanical properties of rubber-modified recycled aggregate concrete.* Construction and Building Materials, 2022. **318**: p. 125970.

52. Yang, Y., et al., *Mode shape identification and damage detection of bridge by movable sensory system.* IEEE Transactions on Intelligent Transportation Systems, 2022. **24**(1): p. 1299-1313 https://doi.org/10.1109/TITS.2022.3151529.

53. Zhang, J.F., et al., *Multi-objective optimization of concrete mixture proportions using machine learning and metaheuristic algorithms.* Construction and Building Materials, 2020. **253**.

54. Schapire, R.E. *The boosting approach to machine learning: An overview*. in *Workshop on Nonlinear Estimation and Classification*. 2001. Berkeley, CA.

55. Yang, X.S. *Firefly Algorithms for Multimodal Optimization*. in *5th International Symposium on Stochastic Algorithms - Foundations and Applications*. 2009. Hokkaido Univ, Sapporo, JAPAN.

56. Baykasoglu, A., A. Oztas, and E. Ozbay, *Prediction and multi-objective optimization of high-strength concrete parameters via soft computing approaches.* Expert Systems with Applications, 2009. **36**(3): p. 6145-6155.